



RESEARCH

# Comparative analysis of nonlinear tuned inerter absorber applied to impact loads

Zijian Yang · Songtao Xue · Demin Feng ·  
Yasuito Sasaki · Liyu Xie

Received: 28 March 2024 / Accepted: 8 July 2024 / Published online: 20 July 2024  
© The Author(s), under exclusive licence to Springer Nature B.V. 2024

**Abstract** This paper proposes a nonlinear tuned inerter absorber to improve the robustness of tuned mass dampers (TMD) for vibration control and achieve a more lightweight device. The conditions under which the system undergoes targeted energy transfer (TET) are analyzed from the point of view of slow-flow dynamics and nonlinear normal mode for a system subjected to impact loading. An optimal design method for the nonlinear stiffness and damping of the device is proposed, inspired by the existence of an energy threshold and the tuned linear system. Moreover, considering the characteristics of inerter as a class of two-terminal mechanical elements, the performance of the device with and without grounded connections is investigated. It is concluded that the design of the nonlinear stiffness enables the system to enter the TET stage of rapid energy transfer and consumption, and the optimization of the damping of the device further improves the performance of the system after the occurrence of

TET. When controlling multi-degree-of-freedom systems, the nonlinear absorber performs better than the corresponding linear absorber when the energy input to a certain mode of the system exceeds the corresponding energy threshold. Furthermore, in relation to this device, the nonlinearity of the ungrounded connection is more easily activated, resulting in a lower energy threshold and more complex dynamic behaviors compared to the grounded approach.

**Keywords** Inerter · Nonlinear energy sink · Targeted energy transfer · Nonlinear normal mode · Connection schemes

## 1 Introduction

Vibration control is a crucial issue in engineering and has attracted the attention of many researchers. In practice, only a small portion of vibrations can be utilized, such as for energy harvesting, monitoring or exploration. Most vibrations in engineering are detrimental. In civil engineering, for example, vibrations induced by earthquakes or wind can lead to problems in structural safety and occupants' comfort. Vibration control systems for vehicle suspensions are key to improving driving comfort in the automotive industry. In the fields of mechanical engineering or aerospace, the working environment of some precision instruments requires very strict vibration control. Passive control is more reliable than active control, which requires an exter-

---

Z. Yang · S. Xue · L. Xie (✉)  
Department of Disaster Mitigation for Structures, Tongji University, Shanghai 200082, People's Republic of China  
e-mail: liyuxie@tongji.edu.cn

S. Xue  
Department of Architecture, Tohoku Institute of Technology, Sendai, Japan

D. Feng  
China Electronics Engineering Design Institute Co., Beijing, People's Republic of China

D. Feng · Y. Sasaki  
FUJITA CORP., Yokohama, Japan

nal energy input. A linear spring-mass damping system called tuned mass damper (TMD) [1,2] is commonly used due to its excellent control performance. The TMD is designed to dissipate energy efficiently by tuning its natural frequency equal to the natural frequency of the structure to be controlled. However, a linear TMD is only effective for a certain frequency or mode of the structure, as it has only one natural frequency. Furthermore, the effectiveness of TMD control is directly proportional to its additional mass. In situations where the structure to be controlled is excessively heavy, such as a high-rise building, or sensitive to the added mass, such as a spacecraft, the TMD must make a trade-off between lightness and performance.

There is already a good alternative to the lightweight of the TMD - inerter. Inerter is a class of two-terminal mass elements where the output force is proportional to the difference in acceleration between the two terminals. Smith [3] first introduced the term to describe the force-current analogy between mechanics and electrical circuits. Later, scholars introduced it into vibration control systems to replace conventional additional mass blocks. In recent years, inerter-based vibration damping systems have been increasingly used in various fields, including automotive suspensions [4,5], building structures [6,7], bridge cables [8], and spacecraft [9]. The current mechanisms for apparent mass amplification of inerter are primarily the ball-screw [6,10], rack-and-pinion [11], fluid [12,13], and electromagnetic inerter [14,15]. Y. Sugimura et al. [10] applied the ball screw type inerter to a real steel building and obtained an apparent mass of 5600t with a real physical mass of 560 Kg. At this stage of research on the theory, design and application of inerter system, linear control system is obviously more mature. But it is still challenging to overcome the limitations of a single control band.

In recent years, with the development of nonlinear dynamics theory and numerical methods, nonlinear absorbers have attracted the interest of more and more researchers. The nonlinear absorber which is called nonlinear energy sink (NES) have been proposed as a solution to the issue of wideband control. Through the dynamical analysis of a linear system with NES attached, Vakakis et al. [16–20] found the existence of irreversible energy transfer from the linear primary system to the NES, which is known as targeted energy transfer (TET). By applying the complexification-averaging method (CxA) [21] and the

multiscale method, Gendelman et al. [22–25] explored the rich dynamic behaviors of the cubic stiffness NES such as bifurcation, quasi-periodic vibration and strongly modulated response (SMR), which are significant in understanding the mechanisms and conditions of TET. Also, researchers have explored various forms of NESs in addition to cubic stiffness NESs. Nucera et al. [26] demonstrated that a vibro-impact NES with additional piecewise-linear oscillator is capable of achieving intermodal interactions between multiple modes. Gendelman et al. [27,28] theoretically and experimentally investigated that a rotating NES with eccentric mass is also capable of achieving energy transfer, but its dynamic behaviors is complex and prone to chaos. Andersen et al. [29] used geometric nonlinearities to implement a nonlinear damped NES and demonstrated that the device can achieve resonant energy capture over a wide frequency band. Wang et al. [30] proposed a way of using geometrically nonlinear track to achieve a nonlinear restoring force and validated that this type of NES has more robustness and a wider frequency control range than TMD. Lu et al. [31] confirmed the effectiveness of track NES in vibration mitigation of a five-story steel frame structure through shaking table tests.

In the field of nonlinear vibration control, some scholars have recognized the benefits of using inerter to achieve mass amplification and are investigating the effectiveness of vibration control by considering the existence of nonlinearities in inerter, or the active addition of nonlinearities. Wang et al. [32] discusses the nonlinear properties of inerter and their impact on vehicle suspension control. Chen et al. [33,34] proposed a kind of inerter-based NES and verified the suppression effect by theoretical and numerical studies. Zhang et al. [35] proposed a new type of inerter - the crank inerter, which has a nonlinear negative stiffness. The analysis showed that the vibration isolator with crank inerter has better performance in terms of force transmission rate and frequency band.

However, there are still great exploration prospects for NES based on lightweighting inerter in terms of theory, design, and application. For instance, the performance comparison of inerter-based NES and linear inerter systems in disparate scenarios or the impact of inerter two-ended connection on the dynamics of the system remain worthy of further investigation. In light of the aforementioned research background, this paper proposes a nonlinear tuned inerter absorber

which is more lightweight than the conventional NES. The dynamic characteristics and performance of the structure equipped with this nonlinear absorber are also compared with that of the linear absorber for impact loading. Based on the conditions under which the system enters the TET and the inspiration of the resonance energy dissipation of the linearly tuned inerter system, a design method for the nonlinear stiffness and damping of the device is proposed. The performance difference between the grounded and ungrounded connection schemes of the inerter in a multi-degree-of-freedom structure is also investigated. The paper is structured as follows: Section 2 presents the mechanical model of the device; Section 3 analyses the nonlinear stiffness design method based on energy threshold from the perspective of invariant manifold. And the performance of the system into the TET is further optimized by compared with the linear absorber; Section 4 explains the existence of the energy threshold from the nonlinear normal mode point of view and illustrates the reason for the high efficiency of NES by comparing it with linear mode; Section 5 explores the effect of different installation methods for the device of the multi-degree-of-freedom system. The final section summarizes the paper’s conclusions.

### 2 Mechanical model

The nonlinear tuned inerter absorber proposed in this paper mainly adopts the mechanical topological form of tuned viscous mass damper (TVMD) proposed by ikago et al. [6]. The main feature of this form is that the damping element and the inerter are connected in parallel, which is conducive to the integration of damping and inerter in the actual device. For example, the flywheel of the ball screw type inerter can be made of conductive material, which can be combined with the magnetic field generated by the permanent magnet to achieve the dual role of inertia amplification and electromagnetic damping as the flywheel rotates. Figure 1 shows the physical schematic of a nonlinear tuned inerter absorber. The device employs the ball screw type inerter to achieve apparent mass amplification by converting the translational motion of the screw in the axial direction into the high-speed rotation of the flywheel. A linear spring is introduced in series with the screw to achieve tuning of the system. In addition, the introduction of cubic stiffness is achieved by geometric

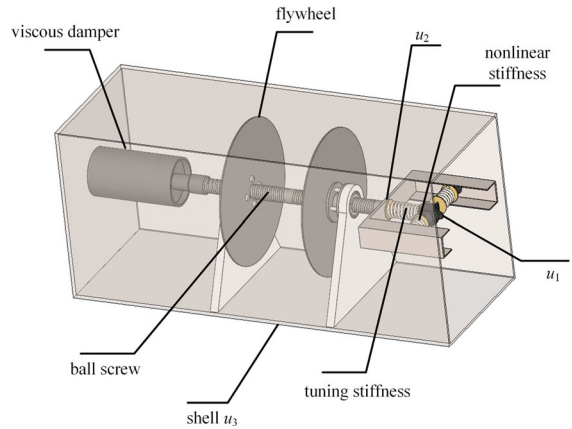


Fig. 1 Physical diagram of the device

non-linearity using a pair of springs placed perpendicular to the axis of the screw. When the screw moves in the axial direction, the spring placed perpendicular to the axis of the screw will have approximately the intrinsic relationship of cubic stiffness. The mechanical model of the device can be simplified as shown in Fig. 2. Figure 3 depicts a comprehensive illustration of the self-balanced inerter utilized by the device. The self-balancing mechanism ensures that the torques generated by the flywheel’s rotational motion are effectively neutralized by the screw. The screw rod with right-hand and left-hand threads are the key to achieving self-balanced inerter. When the screw rod moves in the axial direction, the symmetrical flywheels in different thread directions rotate in opposite directions, balancing the torque applied to the screw rod. This counterbalance relieves the torque constraints required at the end of the screw rod [36]. The apparent mass amplification equation resulting from the inerter is presented in Eq. (1).

$$m_d = m_0 \left( r_0^2 + r_d^2 \right) \left( \frac{2\pi}{l_d} \right)^2 \tag{1}$$

where  $m_0$  is the mass of the flywheel,  $r_0$  and  $r_d$  are the radius of the flywheel and screw rod, respectively, and  $l_d$  is the lead of the ball screw. The rational design of  $r_0$  and  $l_d$  enables the amplification of the flywheel’s mass by a factor of thousands.

The mechanical relationship of the nonlinear tuned inerter absorber is shown as follows:

$$k_d(u_1 - u_2) + k_n(u_1 - u_2)^3 = m_d(\ddot{u}_2 - \ddot{u}_3) + c_d(\dot{u}_2 - \dot{u}_3). \tag{2}$$

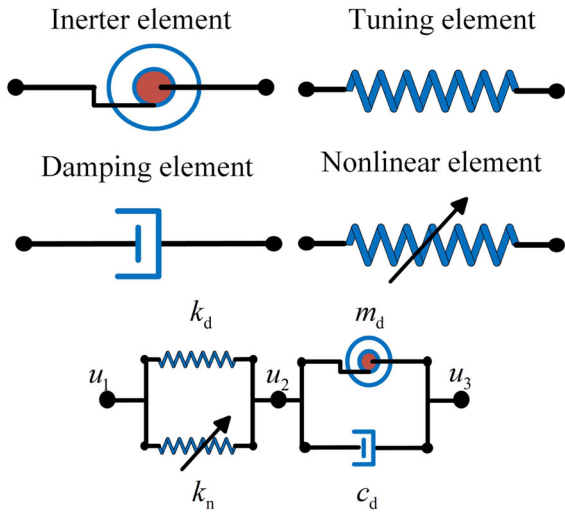


Fig. 2 Simplified mechanical model of the device

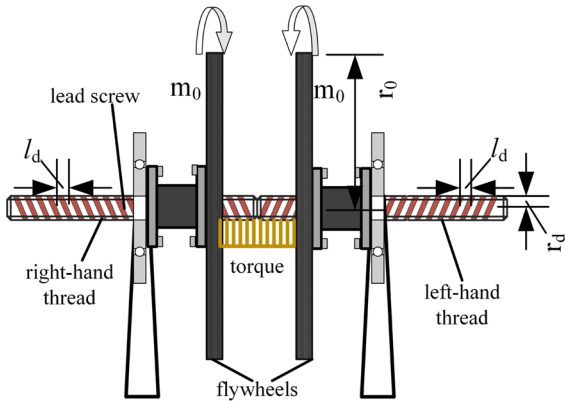


Fig. 3 Self-balanced inerter

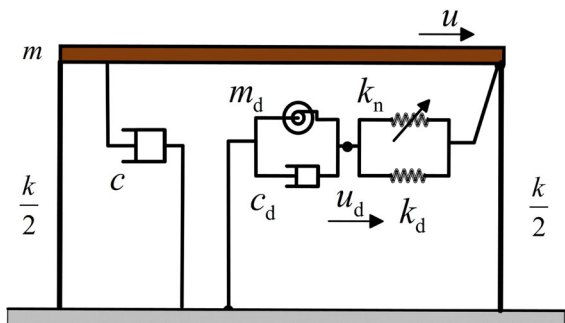


Fig. 4 Schematic diagram of a sdof structure equipped with the nonlinear vibration absorber

As shown in Fig. 4, since the inerter is a class of two-terminal mechanical elements, the application of the device to a single-degree-of-freedom (sdof) structure requires one end to be grounded and the other end to be attached to the structure to be controlled. The equations of motion for such a system can be simplified as follows:

$$\begin{aligned}
 m\ddot{u} + c\dot{u} + ku + k_d(u - u_d) + k_n(u - u_d)^3 &= F \\
 m_d\ddot{u}_d + c_d\dot{u}_d + k_d(u_d - u) + k_n(u_d - u)^3 &= 0
 \end{aligned}
 \tag{3}$$

where  $m$ ,  $c$  and  $k$  are the mass, damping coefficient and stiffness of the primary SDOF system;  $m_d$ ,  $c_d$ ,  $k_d$  and  $k_n$  are the apparent mass, damping coefficient, tuning stiffness and nonlinear stiffness coefficient of the absorber;  $u$  and  $u_d$  represent the main structural displacement and the displacement of one end of the inerter, respectively, while the other end of the inerter is grounded. The apparent mass of the ball-screw inerter used in this device is related to the lead and radius of the screw, as well as the mass and radius of the flywheel, and can be amplified by a factor of several thousand compared to its true physical mass.  $F$  is the external force acting on the primary structure. In this paper, the performance of this absorber is analyzed for impact loading, whereas the external load is applied to the main structure in the form of an initial condition, and therefore  $F$  is equal to zero. After introducing dimensionless time  $\tau = \omega_s t$ , the dimensionless Eq. (3) can be rewritten as follows:

$$\begin{aligned}
 u'' + 2\varepsilon\lambda u' + u + \varepsilon\kappa(u - u_d) &+ \varepsilon\alpha_n(u - u_d)^3 = 0 \\
 \varepsilon u_d'' + 2\varepsilon\lambda_d u_d' + \varepsilon\kappa(u_d - u) &+ \varepsilon\alpha_n(u_d - u)^3 = 0
 \end{aligned}
 \tag{4}$$

The parameters that are newly introduced are defined as follows:

$$\begin{aligned}
 \varepsilon &= \frac{m_d}{m}; \omega_s^2 = \frac{k}{m}; \lambda = \frac{c}{2m_d\omega_s}; \\
 \lambda_d &= \frac{c_d}{2m_d\omega_s}; \kappa = \frac{k_d}{m_d\omega_s^2}; \alpha_n = \frac{k_n}{m_d\omega_s^2}
 \end{aligned}
 \tag{5}$$

where ' the derivative with respect to time  $\tau$ ;  $\varepsilon \ll 1$  stands for the mass ratio of the nonlinear attachment assumed to be small;  $\omega_s$  refer to the natural frequency of the main structure;  $\lambda$  and  $\lambda_d$  are the damping ratios of

master mass and absorber device, respectively;  $\alpha_n$  represents the nonlinear stiffness ratio of the absorber. The small mass ratio assumption suggests that the vibration absorber is suitable for the control of large mass structures, such as high-rise or super high-rise structures, large machinery, etc. In the case of small mass ratios, the mass of the damping device remains considerable, as evidenced by the 1,000-tonne TMD on the Shanghai Tower. The use of inerter can further reduce the mass of the damping device, resulting in cost savings.

### 3 Slow flow dynamic

#### 3.1 Slow invariant manifold

Previous studies [23,37–39] have shown that cubic stiffness NES with similar mechanical topological forms have an initial energy threshold at which targeted energy transfer occurs. This section derives the slow invariant manifold (SIM) of the system to demonstrate the transient dynamic behaviors of a nonlinear tuned inerter absorber. The performance and applications of the system in energy dissipation under impulse loading are explored.

To simplify the subsequent algebraic derivation, new variables are introduced as follows:

$$\begin{cases} x = u + \varepsilon u_d \\ y = u - u_d \end{cases} \tag{6}$$

where  $x$  represents the displacement of the equivalent center of mass of the system considering the apparent mass of the inerter rather than the real physical mass;  $y$  represents the relative displacement. By substituting the new variables into Eq. (4) and omitting the second and higher order terms of the  $\varepsilon$ , the equation is as follows:

$$\begin{aligned} x'' + 2\varepsilon\lambda x' + x + \varepsilon y'' + \varepsilon(1 + \kappa)y \\ + \varepsilon\alpha_n y^3 + \mathcal{O}(\varepsilon^2) = 0 \\ \varepsilon y'' + 2\varepsilon\lambda_d y' + \varepsilon\kappa y + \varepsilon\alpha_n y^3 - \varepsilon x'' \\ - 2\varepsilon\lambda_d x' + \mathcal{O}(\varepsilon^2) = 0 \end{aligned} \tag{7}$$

Complex variable averaging method is applied to analyze the slow dynamical behaviors of the system, assuming that the system vibrates in a 1:1 resonant mode. The following two complex variables are introduced:

$$\begin{aligned} \varphi_0(t)e^{it} = x' + ix, \quad \varphi_0 \in \mathbb{C} \\ \varphi_1(t)e^{it} = y' + iy, \quad \varphi_1 \in \mathbb{C} \end{aligned} \tag{8}$$

where  $\varphi_0(t)$  and  $\varphi_1(t)$  are time-dependent slow modulation functions, representing the slow-varying amplitude and slow-varying phase of the system. The above complex variables are extended to the series expansion of  $\varepsilon$  and the multiscale method is used to separate the fast and slow time terms in the complex variables as follows:

$$\begin{aligned} \varphi_i = \varphi_{i,0} + \varepsilon\varphi_{i,1} + \mathcal{O}(\varepsilon^2), \quad \forall i = 0..1 \\ \tau_k = \varepsilon^k t, \quad \frac{d}{dt} = \frac{\partial}{\partial\tau_0} + \varepsilon \frac{\partial}{\partial\tau_1} + \mathcal{O}(\varepsilon^2) \end{aligned} \tag{9}$$

Substituting Eqs. (8) and (9) into Eq. (7) and ignoring the secular term and omitting the second and higher order terms of the  $\varepsilon$ , the following relationship is satisfied on the  $\tau_0$  and  $\tau_1$  time scale:

$$\begin{aligned} \frac{\partial\varphi_{0,0}}{\partial\tau_0} = 0 \Rightarrow \varphi_{0,0} = \varphi_{0,0}(\tau_1, \tau_2, \dots) \\ 3i\alpha_n\varphi_{1,0}^2\overline{\varphi_{1,0}} - 8\lambda\varphi_{0,0} - 8\frac{\partial\varphi_{0,1}}{\partial\tau_0} \\ - 8\frac{\partial\varphi_{1,0}}{\partial\tau_0} - 8\frac{\partial\varphi_{0,0}}{\partial\tau_1} + 4i\kappa\varphi_{1,0} = 0 \\ 8\lambda_d\varphi_{0,0} - 8\lambda_d\varphi_{1,0} + 4i\kappa\varphi_{1,0} \\ - 4i\varphi_{1,0} + 4i\varphi_{0,0} + 3i\alpha_n\varphi_{1,0}^2\overline{\varphi_{1,0}} \\ + 8\frac{\partial\varphi_{0,0}}{\partial\tau_0} - 8\frac{\partial\varphi_{1,0}}{\partial\tau_0} = 0 \end{aligned} \tag{10}$$

Consider the system that evolves on the  $\tau_1$  time scale while reaching a steady state on the  $\tau_0$  time scale. This approach has been justified in the literature [23]. Equation (10) can be expressed as follows:

$$\begin{aligned} \frac{\partial\varphi_{0,0}}{\partial\tau_0} = 0 \Rightarrow \varphi_{0,0} = \varphi_{0,0}(\tau_1, \tau_2, \dots) \\ 3i\alpha_n\varphi_{1,0}^2\overline{\varphi_{1,0}} - 8\omega_s^4\lambda\varphi_{0,0} \\ - 8\frac{\partial\varphi_{0,0}}{\partial\tau_1} + 4i\kappa\varphi_{1,0} = 0 \\ 8\lambda_d\varphi_{0,0} - 8\lambda_d\varphi_{1,0} + 4i\kappa\varphi_{1,0} \\ - 4i\varphi_{1,0} + 4i\varphi_{0,0} + 3i\alpha_n\varphi_{1,0}^2\overline{\varphi_{1,0}} \\ = 0 \end{aligned} \tag{11}$$

Rewrite the complex variable in polar form as follows:

$$\varphi_{0,0} = R_0(\tau_1)e^{i\theta_0(\tau_1)}; \quad \varphi_{1,0} = R_1(\tau_1)e^{i\theta_1(\tau_1)} \tag{12}$$

Substituting Eq. (12) into Eq. (11) and separating the real and imaginary parts yields the following relationship:

$$\begin{cases} 4 \sin(\theta_0 - \theta_1) \kappa R_1 - 8\lambda R_0 \\ \quad + 3 \sin(\theta_0 - \theta_1) \alpha_n R_1^3 - 8 \frac{\partial R_0}{\partial \tau_1} = 0 \\ 4 \cos(\theta_0 - \theta_1) \kappa R_1 + 3 \cos(\theta_0 - \theta_1) \alpha_n R_1^3 \\ \quad - 8 R_0 \frac{\partial \theta_0}{\partial \tau_1} = 0 \\ 8 \cos(\theta_0 - \theta_1) \lambda_d R_0 - 4 \sin(\theta_0 - \theta_1) R_0 \\ \quad - 8 \lambda_d R_1 = 0 \\ 8 \sin(\theta_0 - \theta_1) \lambda_d R_0 + 4 \cos(\theta_0 - \theta_1) R_0 \\ \quad + 4(\kappa - 1) R_1 - 3 \alpha_n R_1^3 = 0 \end{cases} \quad (13)$$

The modulus relation can be obtained by algebraically transforming Eq. (13) to eliminate the phase  $\theta_0$  and  $\theta_1$  as follows:

$$\begin{aligned} R_0^2 &= \\ & \frac{R_1^2 \left( (3R_1^2 \alpha_n + 4(\kappa - 1))^2 + 64\lambda_d^2 \right)}{16(4\lambda_d^2 + 1)} \\ \frac{\partial R_0}{\partial \tau_1} &= \\ & - \frac{16(4\lambda_d^2 + 1)\lambda R_0^2 + \lambda_d R_1^2 (3\alpha_n R_1^2 + 4\kappa)^2}{16R_0(4\lambda_d^2 + 1)} \end{aligned} \quad (14)$$

Variable substitution is considered by using energy-like state variables  $E_i = R_i^2, \forall i = 0, 1$ .

$$\begin{aligned} E_0 &= \frac{E_1 \left( (3E_1 \alpha_n + 4(\kappa - 1))^2 + 64\lambda_d^2 \right)}{16(4\lambda_d^2 + 1)} \\ \frac{\partial E_0}{\partial \tau_1} &= \\ & - \frac{16(4\lambda_d^2 + 1)\lambda E_0 + \lambda_d E_1 (3\alpha_n E_1 + 4\kappa)^2}{8(4\lambda_d^2 + 1)} \end{aligned} \quad (15)$$

$E_0$  and  $E_1$  can represent approximately the energy levels of the new variables in Eq. (9) in the multiscale method analysis. Equation(15) demonstrates the invariant manifold and the evolutionary relationships of the system on slow time scale  $\tau_1$ . The first equation in system (15) shows a cubic non-linear relationship that exists between  $E_0$  and  $E_1$ . The second equation in system (15) shows the decay of  $E_0$  with time scale  $\tau_1$  in relation to  $E_0$  and  $E_1$ . A comparison with previous studies [37–39] revealed that the inerter-based NES has a similar SIM structure to the conventional cubic stiffness NES. This finding suggests that the device can be used as a lightweight alternative to the conventional cubic stiffness NES.

### 3.2 Parametric analysis and design

Several works have demonstrated the existence of conditions for cubic stiffness NES with a similar invariant manifold to enter the TET, which can be summarized as the following two main conditions: i, there is a bifurcation of the invariant manifold of the system, in particular, for a given state of  $E_0$  there are multiple states of  $E_1$  that correspond to it; and ii, for the transient energy dissipation of the system, the initial energy of  $E_0$  must be greater than a certain energy threshold. This section focuses on the bifurcation conditions and energy threshold of the proposed nonlinear tuned inerter absorber device into the TET and is verified by numerical simulations.

For the invariant manifold in system (15), the relationship between  $E_0$  and  $E_1$  is a cubic function. If there are extreme points ( $E_1 > 0$ ) in this function, a multiple solution situation exists. This function is now derived as follows:

$$\frac{\partial E_0}{\partial E_1} = \frac{(6\alpha_n E_1 + 4(\kappa - 1)^4)^2 + 64\lambda_d^2 - 9\alpha_n^2 E_1^2}{16(4\lambda_d^2 + 1)} \quad (16)$$

The conditions for the existence of extreme points are as follows:

$$\lambda_d < \frac{1 - \kappa}{2\sqrt{3}} \quad (17)$$

The extrema of  $E_0$  and  $E_1$  are:

maximum:

$$\begin{aligned} E_1^+ &= \frac{4(2(1 - \kappa) - \sqrt{(\kappa - 1)^2 - 12\lambda_d^2})}{9\alpha_n} \\ E_0^+ &= \frac{E_1^+ \left( (3E_1^+ \alpha_n + 4(\kappa - 1))^2 + 64\lambda_d^2 \right)}{16(4\lambda_d^2 + 1)} \end{aligned} \quad (18)$$

minimum:

$$\begin{aligned} E_1^- &= \frac{4(2(1 - \kappa) + \sqrt{(\kappa - 1)^2 - 12\lambda_d^2})}{9\alpha_n} \\ E_0^- &= \frac{E_1^- \left( (3E_1^- \alpha_n + 4(\kappa - 1))^2 + 64\lambda_d^2 \right)}{16(4\lambda_d^2 + 1)} \end{aligned} \quad (19)$$

Figure 5 illustrates two cases of invariant manifolds in the presence and absence of bifurcation. Previous studies [37–39] have confirmed that  $E_0^+$  is the energy threshold for transient energy dissipation of the system into the TET. Figure 6 reveals that two other possible energy pumping situations occur after ignoring the

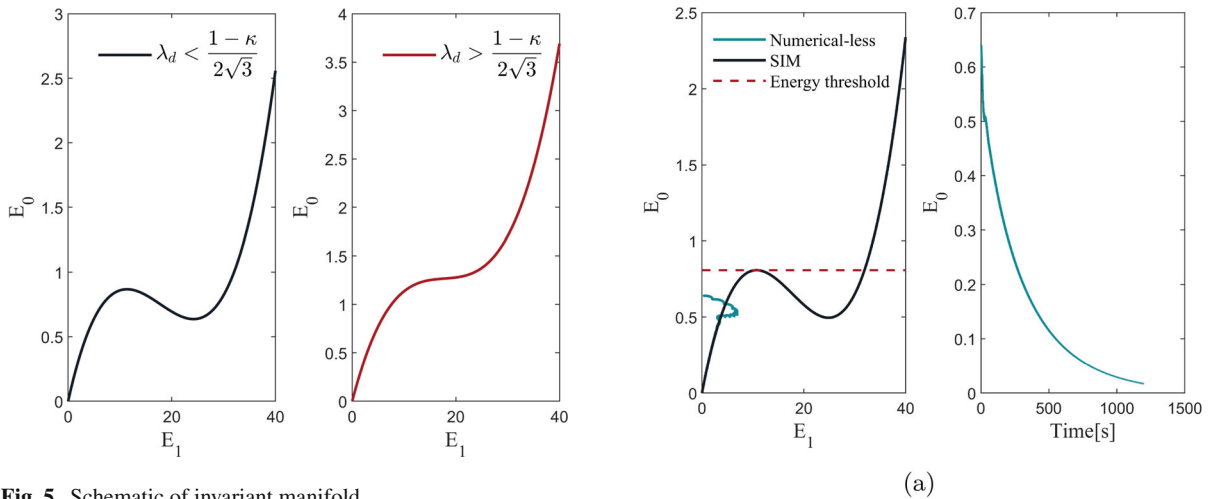


**Fig. 5** Schematic of invariant manifold

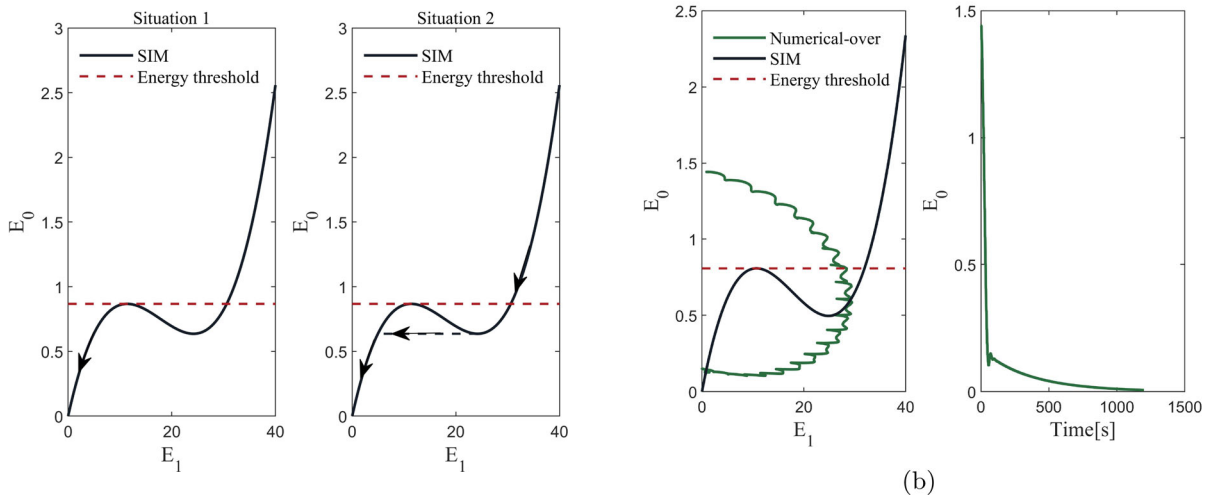


**Fig. 6** Different energy pump situations

**Fig. 7** Numerical simulation of energy transfer and dissipation in different situations. **a** Less initial energy; **b** over initial energy

unstable energy pumping case, corresponding to the invariant manifold of the system, where the left corresponds to an initial value of  $E_0(0)$  lower than  $E_0^+$  and the right corresponds to  $E_0(0)$  higher than  $E_0^+$ . And case b is the evolutionary trajectory that optimally happens, because the system enters the TET stage, which is able to rapidly dissipate the transient energy input into the main system. The reason for this phenomenon is revealed by the second equation of system(15). When situation b occurs, the system is attracted to the right branch of the invariant manifold. The energy  $E_1$  of the right branch is significantly larger, which favors the decay of  $E_0$ .

Figure 7 illustrates the relationship of energy transfer for  $E_0$  and  $E_1$ (left) and the decay of  $E_0$  over time

(right) at different initial energy levels where the values of each parameter for the numerical simulation are taken as follows:  $\omega_s = 1, \lambda = 0, \epsilon = 0.01, \kappa = 0.6, \lambda_d = 0.08, \alpha_n = 0.02$ . The numerical simulation is carried out with the following initial conditions: a,  $\dot{u} = 1.2$ ; b,  $\dot{u} = 0.8$ . The rest of the state variables are initially set to 0. It can be observed that the numerical results are in better agreement with the theoretical results when following the left branch of the invariant manifold. Whereas when the initial energy exceeds the energy threshold, the numerical values differ more from the theoretical results, taking into account the approximate treatment in the derivation process. But there is

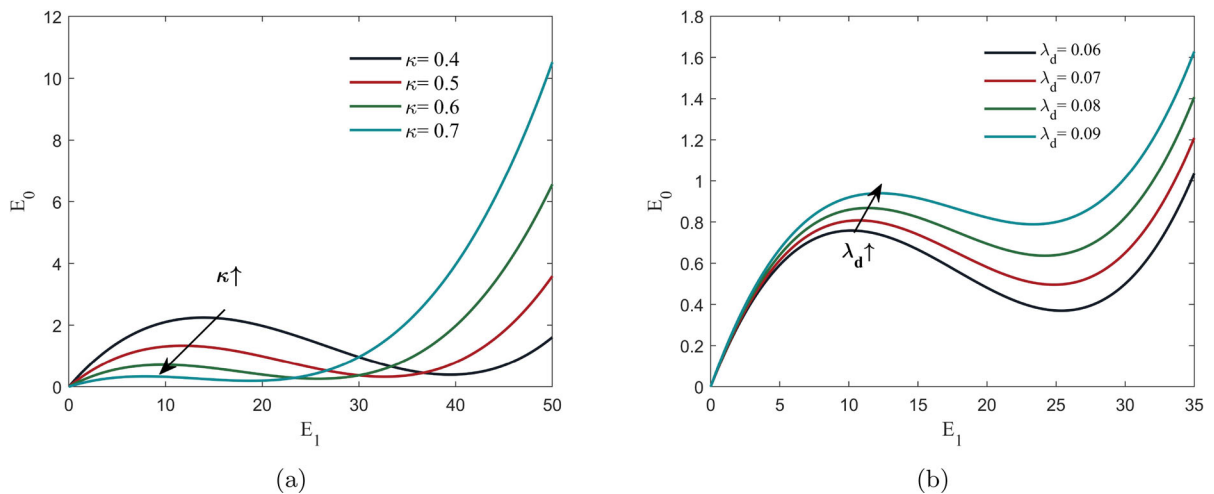


**Fig. 8** The effect of parameter variation on invariant manifold. **a** Tuned stiffness ratio; **b** damping ratio

also a process of being attracted to the right branch of the invariant manifold. In this case, the decay of the main structure energy with time is significantly accelerated compared to the low initial energy case.

Figure 8 shows the effect on the invariant manifold of varying the damping ratio and tuned stiffness ratio of the nonlinear tuned inerter absorber. The reduction of the tuning stiffness ratio  $\kappa$  effectively decreases the energy threshold for the occurrence of TET, but also decreases the energy level  $E_1$  of the right branch of the invariant manifold which has a detrimental effect on the suppression of the energy of the main structure. Similarly, the reduction of the damping ratio  $\lambda_d$  is also effective in reducing the energy threshold. However, the second equation of system (15) reveals that reducing the damping ratio can reduce the coefficient of influence of  $E_1$  on the decay rate of the main structure. And the variations in  $\kappa$  and  $\lambda_d$  are limited by Eq. (17).

Substitute the new variables  $Z_0 = \alpha_n E_0$  and  $Z_1 = \alpha_n E_1$  into Eq. (15) as follows:

$$Z_0 = \frac{Z_1 \left( (3Z_1 + 4(\kappa - 1))^2 + 64\lambda_d^2 \right)}{16(4\lambda_d^2 + 1)}$$

$$\frac{\partial Z_0}{\partial \tau_1} = - \frac{16(4\lambda_d^2 + 1)\lambda Z_0 + \lambda_d Z_1 (3Z_1 + 4\kappa)^2}{8(4\lambda_d^2 + 1)} \tag{20}$$

The energy threshold corresponding to the new variable  $Z_0$  is as follows:

$$Z_1^+ = \frac{4(2(1 - \kappa) - \sqrt{(\kappa - 1)^2 - 12\lambda_d^2})}{9}$$

$$Z_0^+ = \frac{Z_1^+ \left( (3Z_1^+ + 4(\kappa - 1))^2 + 64\lambda_d^2 \right)}{16(4\lambda_d^2 + 1)} \tag{21}$$

To ensure the occurrence of TET for the transient energy dissipation of the system, the following equation must be satisfied:

$$\alpha_n E_0(0) > Z_0^+ \Rightarrow \alpha_n > \frac{Z_0^+}{E_0(0)} \tag{22}$$

where

$$E_0(0) \cong x'(0)^2 + x(0)^2 \tag{23}$$

The values of  $x'(0)$  and  $x(0)$  correspond to their respective initial values. The primary structure decays fastest when the initial energy  $E_0(0)$  of the system is only slightly higher than  $E_0^+$ . It can be seen from Eq. (22) that a reasonable design of non-linear stiffness, which is based on the magnitude of the impact loads that the primary structure may be subjected to, will ensure that the TET occurs and thus increase the rate of its energy dissipation.



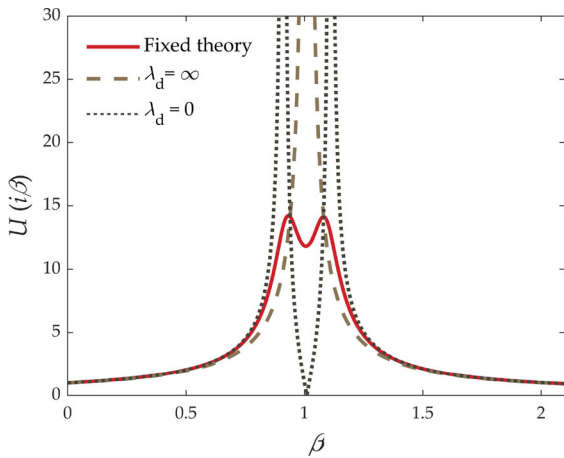


Fig. 9 Schematic diagram of fixed-point theory

### 3.3 Performance comparison with linear system

This section compares the invariant manifolds of the nonlinear tuned inerter system with the corresponding linear systems to optimize the design. There are two comparisons of the corresponding linear system: one is the derived system where the nonlinear stiffness is zero and the rest of the parameters are the same as the nonlinear system, and the other is the linear system tuned by fixed-point theory method [6,40]. Figure 9 shows the method of fixed-point theory optimization, where the damping and stiffness ratios of the linear inerter system are optimally tuned to maximize and equalize the values of the displacement transfer function of the main structure at a pair of fixed points. This method can control the resonance response of the main structure very well, which makes it more suitable for controlling impact loads. The values of the damping ratio and the tuning stiffness ratio of the linear system optimized by the fixed-point theory are given in the following equation:

$$\begin{cases} \lambda_1^{\text{opt}} = \frac{1}{2} \sqrt{\frac{3\varepsilon}{(1-\varepsilon)(2-\varepsilon)}} \\ \kappa_1^{\text{opt}} = \frac{1}{1+\varepsilon} \end{cases} \quad (24)$$

where  $\varepsilon$ ,  $\lambda_1^{\text{opt}}$  and  $\kappa_1^{\text{opt}}$  are the mass ratio, damping ratio and tuning stiffness ratio of the linear system obtained by fixed-point theory optimization, respectively, with the same definitions as before.

The parameter values  $\omega_s = 1$ ,  $\lambda = 0$ ,  $\varepsilon = 0.01$ ,  $\kappa = 0.6$ ,  $\lambda_d = 0.08$ ,  $\alpha_n = 0.02$  are used as an example to obtain the invariant manifolds of the nonlinear tuned inerter system. At the same time, it is compared with

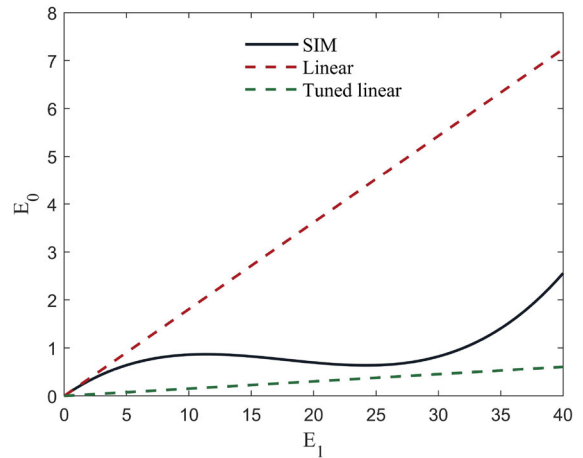


Fig. 10 Comparison of invariant manifolds for nonlinear and linear systems

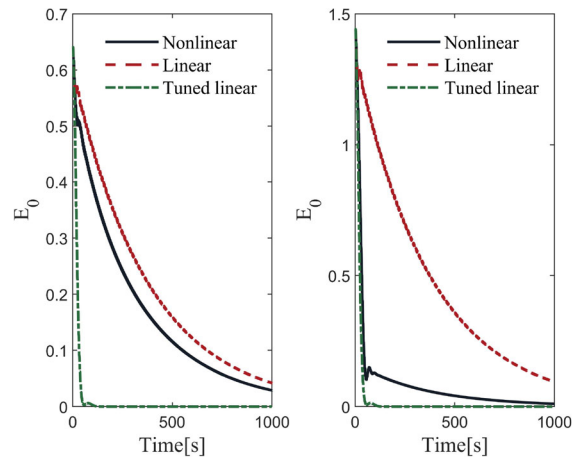
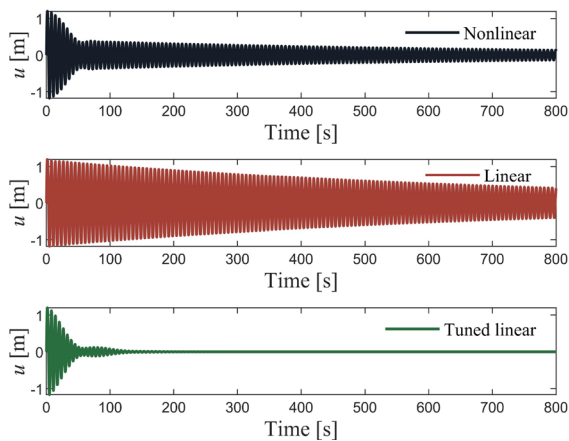


Fig. 11 Comparison of primary structure energy consumption. (left)less initial energy; (right)over initial energy

the invariant manifolds of the derived system and tuned linear system, as shown in Fig. 10, where the invariant manifolds of the linear system are obtained by setting  $\alpha_n$  in Eq. (15) to 0 as shown in Eq. (25). The values of the tuned linear system parameters are given by Eq. (24).

$$E_0 = \frac{(\kappa - 1)^2 + 4\lambda_d^2}{4\lambda_d^2 + 1} E_1 \quad (25)$$

Figure 10 shows that the invariant manifold of the linearly derived system is exactly the tangent to the SIM of the nonlinear system at the origin. This demonstrates that the nonlinear tuned inerter absorber behaves linearly when the energy level of the system is not high. In contrast, the invariant manifold of the optimized linear system has a much smaller gradient, meaning that



**Fig. 12** Comparison for displacement control of the primary structure under high initial energy inputs

for the same  $E_0$ , the corresponding  $E_1$  is larger and more conducive to energy dissipation of the primary system. Figures 11 and 12 illustrates the effect of the three control systems on the primary structure for the two initial conditions in the previous section. The tuned linear system is observed to have the best control effect on the single degree of freedom structure for different initial conditions which is consistent with the scenario envisaged, as the tuned linear control system provides excellent control of the resonance peaks of the s dof structure. When the initial energy input is low, the non-linear system behaves consistently with its derived system in terms of energy dissipation. However, when the initial energy input is high, the nonlinear system undergoes the TET, which results in a much faster rate of energy dissipation of the primary structure compared with the derived system.

### 3.4 Optimized design of damping coefficients

The above analysis provides the insight to optimize the non-linear tuned inerter system, which means that when the energy level of the input system is not high, its characteristics can be approached towards the optimized linear system. However, it is found that Eqs. (17) and (24) cannot be satisfied simultaneously, which indicates that linear resonant energy dissipation at low initial energy input and TET at high initial energy input cannot occur simultaneously. Consequently, the design is optimized using a compromise approach. The other tangent equation to calculate the non-linear system SIM

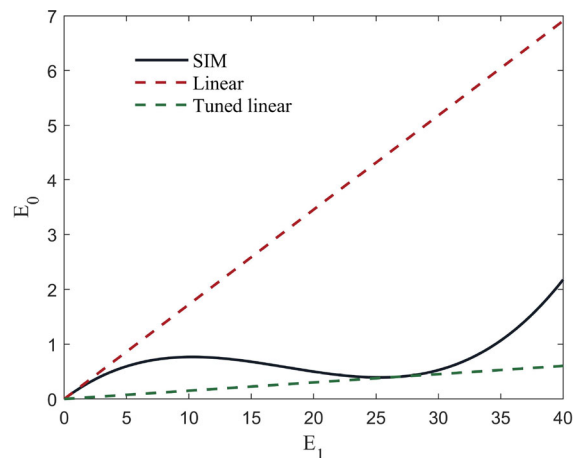


**Fig. 13** Comparison of invariant manifolds for nonlinear and linear systems (optimized nonlinear damping)

through the origin is given in the following equation:

$$E_0 = \frac{4\lambda_d^2}{4\lambda_d^2 + 1} E_1 \quad (26)$$

The previous analysis indicates that a moderate value of the damping ratio  $\lambda_d$  is favorable for the decay of the primary structure energy. Equation (26) demonstrates that the other tangent equation of SIM over the origin is solely dependent on the damping ratio of the nonlinear tuned inerter absorber, and its slope increases with the damping ratio. The trade-off here is to make the tangent equation expressed in Eq. (26) the same as the equation expressed in Eqs. (24) and (25) for tuned linearity to obtain a value for the damping ratio of the non-linear system. The optimized values of damping ratio  $\lambda_d^{\text{opt}}$  is taken as follows:

$$\lambda_d^{\text{opt}} = \frac{\sqrt{(2\varepsilon^3 - 5\varepsilon^2 + \varepsilon + 2) \varepsilon (\varepsilon^3 + 8\varepsilon + 3)}}{2(2\varepsilon^3 - 5\varepsilon^2 + \varepsilon + 2)} \quad (27)$$

Figure 13 illustrates the invariant manifolds of various systems. It can be observed that the tuned linear system is in tangential contact with the SIM of the nonlinear system, which aligns with the a priori objective. Figures 14 and 15 demonstrate the effect of the energy dissipation of the primary structure. The nonlinear tuned inerter absorber exhibits an enhanced performance, which is equivalent to the tuned linear system in terms of its behavior at high initial energy inputs.

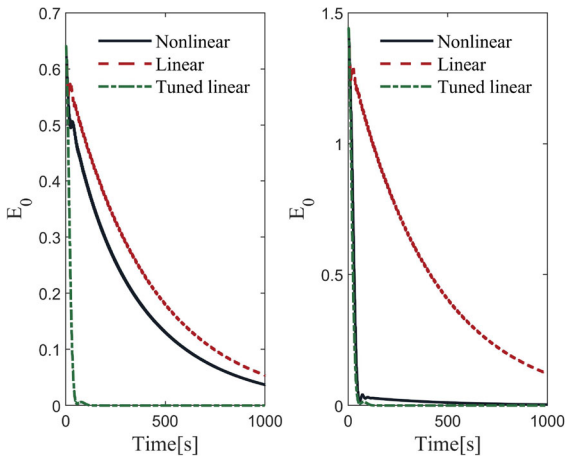


**Fig. 14** Comparison of primary structure energy consumption (optimized nonlinear damping). (left)less initial energy; (right)over initial energy

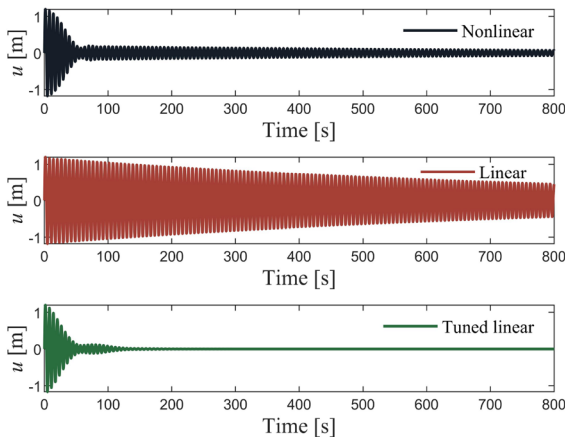


**Fig. 15** Comparison for displacement control of the primary structure under high initial energy inputs (optimized nonlinear damping)

#### 4 Comparison of nonlinear normal mode and linear mode

This section focuses on nonlinear normal mode (NNM) to explain the reason for the large difference in the performance of the nonlinear tuned inerter absorber due to the different initial conditions in Sec. 3 There are two main definitions of nonlinear modes: i Rosenberg’s definition [41,42]; ii Shaw and Pierre’s definition [43,44]. Shaw and Pierre extended Rosenberg’s definition by the invariant manifold method to make it suitable for non-conservative systems. The NNM of a system can be approximated to characterize its transient

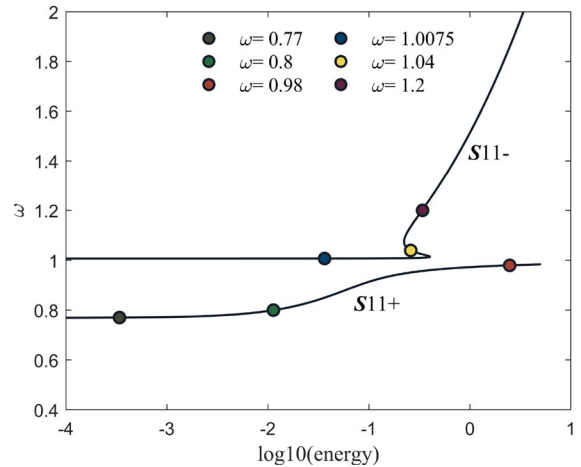


**Fig. 16** Schematic for the FEP of the system

damped dynamical behaviors [45] which allows the behaviors of the system to be explained and predicted to some extent. Due to the frequency-energy dependence of the NNM, the frequency-energy plot (FEP) is a convenient description method [18]. In this paper, the FEP of the system is obtained using the harmonic balance method and the parametric continuation scheme [46–48]. In this section, the harmonic balance method (HBM) uses 7th order harmonics to approximate the motion of the system. And alternating frequency-time technique is used to simplify the calculation of nonlinear force Fourier coefficients. The system parameters are determined according to the optimization method described in the preceding sections as  $\omega_s = 1, \lambda = 0, \varepsilon = 0.01, \kappa = 0.6, \lambda_d = 0.0619, \alpha_n = 0.02$ . The FEP of the system is shown in Fig. 16.

The fundamental FEP backbone curves  $S11+$  and  $S11-$  are shown in Fig. 16. For  $S_{nm\pm}$ ,  $S$  denotes symmetry and  $nm$  denotes the resonance frequency ratio ( $n:m$ ) between the primary structure and the NES, where the plus sign (+) indicates in phase and the minus sign (–) indicates anti-phase motions. Figure 17 illustrates the periodic motion of some representative points on the FEP and the corresponding configuration diagrams. The vibrational energy is mainly concentrated on the NES on some branches which favor the energy dissipation of the main system. A time-frequency analysis method (continuous wavelet transform) is used to calculate the instantaneous spectra for the two different initial conditions in Sec. 3, and the instantaneous spectra are mapped onto the frequency-energy plot by

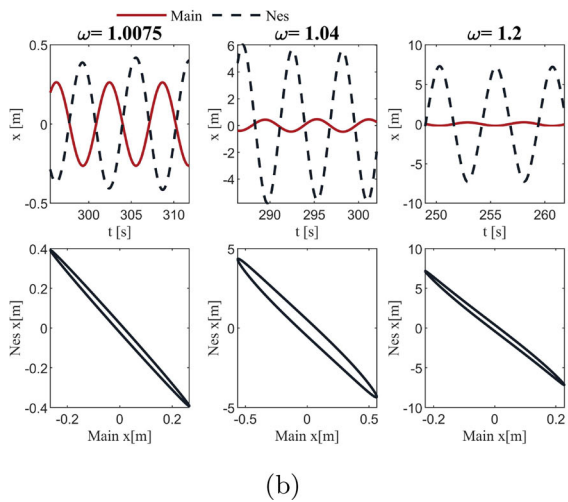
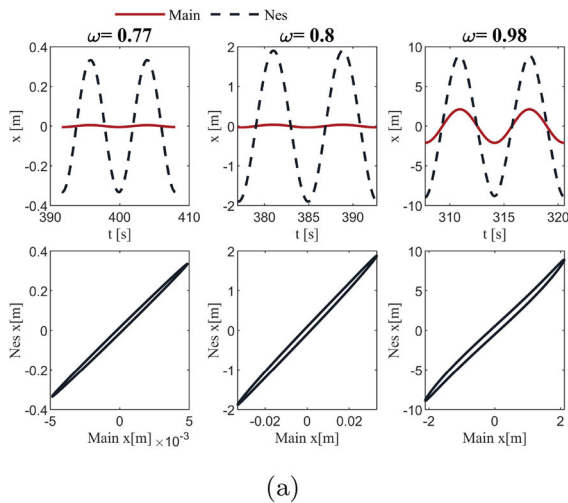


**Fig. 17** Schematic periodic motion and configuration diagram of NNM corresponding to frequency

means of the correspondence between the total energy of the system and time. For comparison, the same analysis is carried out for the linearly derived system.

Figures 18 and 19 show the results of the analyses for the two initial conditions, respectively. Figures 18b and 19b show that for the derived system, its FEP is two straight lines, corresponding to the two modes of the linear system, and its spectrum does not change with the variation of the initial conditions. Figures 18a and 19a show the spectral analysis of the non-linear system. When the initial energy input is low, its instantaneous spectrum is basically the same as that of its derived system. When the initial energy input is high, the instantaneous spectrum varies and concentrates more on the

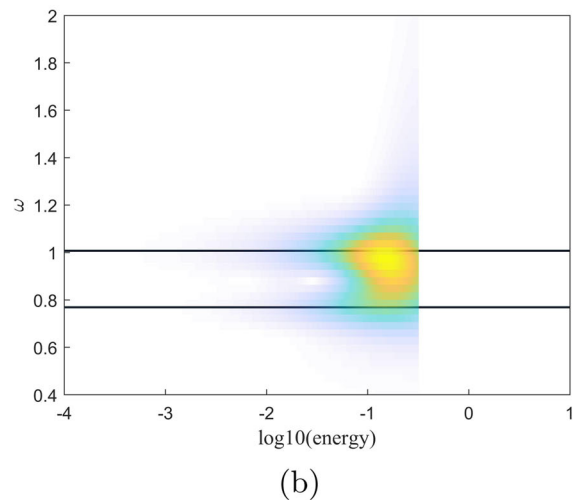
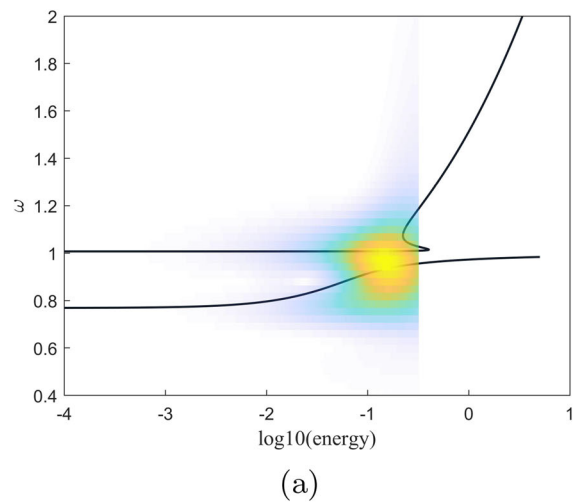
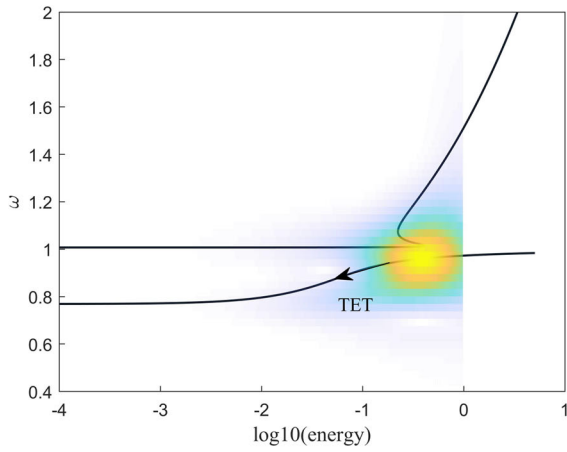
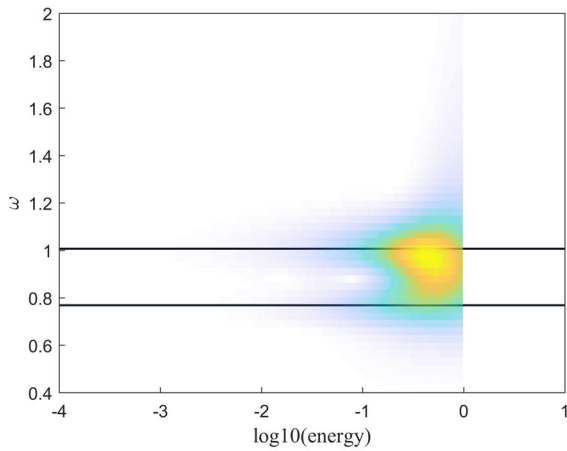


**Fig. 18** Time-frequency analysis at low initial energy input:  $u_d = 0.8\text{m/s}$ . **a** Nonlinear systems; **b** derived systems

$S_{11+}$  branch. It can be seen that the energy extremum on the  $S_{11-}$  branch corresponds to the energy threshold of the SIM, and when the initial energy exceeds this extremum, the systems are attracted to the  $S_{11+}$  branch. In the configuration diagram shown in Fig. 17, the amplitude of the  $S_{11+}$  NES is much larger than that of the primary structure, thus favoring the energy dissipation of the main system. In contrast to a linear system, the introduction of non-linearities can lead to localization phenomena in the system, which means that the energy is mainly concentrated locally in the system. In this case, the energy is concentrated in the NES, thus favoring the control of the dynamic response of the main structure.



(a)



(b)

**Fig. 19** Time-frequency analysis at high initial energy input:  $u_d = 1.2\text{m/s}$ . **a** nonlinear systems; **b** derived systems

### 5 Multi-modal energy consumption analysis

#### 5.1 Ground connection scheme

This section explores the performance of a non-linearly tuned inerter absorber applied to a multi-degree-of-freedom (MDOF) system. As shown in Fig. 20, a three-degree-of-freedom system is used as an illustration in this paper, with one end of the absorber connected to the top degree of freedom and the other end grounded. The equations of motion of the system are as Eq. (28).

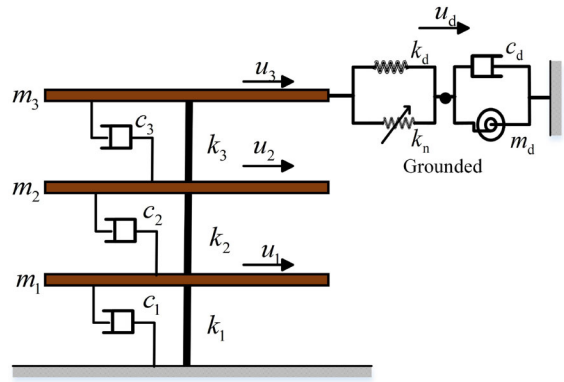


**Fig. 20** Schematic diagram of a multi-degree-of-freedom system

$$\mathbf{M}\ddot{\mathbf{u}} + \mathbf{C}\dot{\mathbf{u}} + \mathbf{K}\mathbf{u} + f_n(\mathbf{u}, u_d)\mathbf{h} = 0$$

$$f_n(\mathbf{u}, u_d) = k_d(\mathbf{h}^T \mathbf{u} - u_d) + k_n(\mathbf{h}^T \mathbf{u} - u_d)^3 \quad (28)$$

$$= m_d \ddot{u}_d + c_d \dot{u}_d$$

where  $\mathbf{M}$ ,  $\mathbf{C}$  and  $\mathbf{K}$  are the mass, damping and stiffness matrices of the MDOF system, respectively;  $\mathbf{u}$  is the displacement vector of the system;  $f_n(\mathbf{u}, u_d)$  is the non-linear force of the absorber; and  $\mathbf{h}$  is the displacement transformation vector with respect to the installation position of the absorber in the system, where  $\mathbf{h}$  takes  $[0, 0, 1]$  for the installation method shown in Fig. 20.

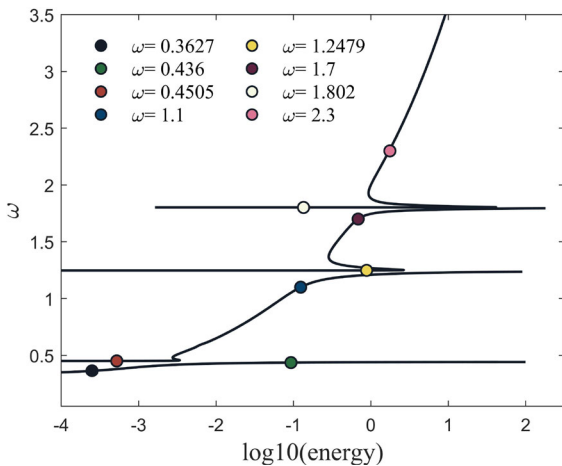
To analyze the effect of non-linear vibration absorbers on a MDOF system subjected to an impact load, the harmonic balance method and the parametric continuation scheme are used to calculate the NNM of the system shown in Eq. (28). In this case, the mass of the non-linear absorber is chosen to be 1% of the total mass of the structure to be controlled. And the rest of the parameters are obtained by using the optimal design methodology in the previous sections, after simplifying this multi-degree-of-freedom structure into an equivalent single-degree-of-freedom system corresponding to the first mode. The values of the parameters for the numerical simulation of system (28) are given in the Table 1.

The damping matrix of the example structure are taken as follows:

$$\mathbf{C} = \alpha_1 \mathbf{M} + \alpha_2 \mathbf{K} \quad (29)$$

**Table 1** Numerical values for MDOF and absorber system

$m_i$ (kg)	$k_i$ (N/m)	$m_d$ (kg)	$c_d$ (Ns/m)	$k_d$ (N/m)	$k_n$ (N/m <sup>3</sup> )
1	1	0.03	0.0017	0.0036	0.006

**Fig. 21** The FEP for multi-degree-of-freedom systems equipped with grounded vibration absorbers

In Eq. (29), the Rayleigh damping assumption is employed, where the first and third modes of the system are assumed to have a damping ratio of 0.05 to obtain  $\alpha_1$  and  $\alpha_2$ .

Figure 21 shows the backbone curves of the frequency-energy plot obtained by the calculation. It can be seen that the structure of the curve is similar at the corresponding linear natural frequency of the derived system: it starts with a straight line and then the total energy decreases, the vibration frequency increases and then the self-oscillation frequency increases with the increase in total energy. Figure 22 shows the periodic motion and configuration diagrams of the NNM at specific frequencies. The vibration absorber's amplitude corresponding to the straight section on the FEP is mostly smaller, indicating that the NES dissipates less energy. The amplitude of the vibration absorber at the curved section of the FEP is larger, which is more beneficial for the energy transfer and dissipation of the primary structure.

In order to better demonstrate the effect of nonlinear tuned inerter absorbers on the control of the multi-degree-of-freedom structure subjected to impact loading, two metrics, the main structure energy con-

sumption ratio  $\gamma_E$  and the absorber energy ratio  $\gamma_d$ , are defined as follows:

$$E = \frac{1}{2} \mathbf{u}^T \mathbf{K} \mathbf{u} + \frac{1}{2} \dot{\mathbf{u}}^T \mathbf{M} \dot{\mathbf{u}}$$

$$E_d = \frac{1}{2} k_d (u_3 - u_d)^2 + \frac{1}{2} m_d \dot{u}_d^2 + \frac{1}{4} k_n (u_3 - u_d)^4 \quad (30)$$

$$\gamma_E = \frac{E}{E(0)}, \quad \gamma_d = \frac{E_d}{E + E_d}$$

where  $E$  is the energy of the primary structure;  $E(0)$  is the energy of the primary structure at the initial moment;  $E_d$  is the energy of the absorber.

Numerical simulations are then performed under different initial conditions to verify the energy dissipation of the system's transient motion in each part of the frequency-energy plot.

Figure 23 (left) shows four representative energy dissipation scenarios for different initial conditions. It can be seen that the results of the time-frequency analysis basically agree with the curve part of the frequency-energy diagram. Figure 23 (right) also shows the relationship between  $\gamma_E$  and  $\gamma_d$  over time. For situation 1, the nonlinear absorber has slightly worse control of the primary structure energy than the corresponding linear absorber. For situation 2 and 3, the nonlinear absorber has a better performance compared to the linear absorber in the early phase. For situation 4, despite the high energy contribution of the nonlinear absorber, the energy oscillation phenomenon occurs, resulting in large oscillations in the primary structure energy, which is detrimental to the dissipation of the primary structure energy. The combination of the four scenarios reveals that the energy dissipation of the system is consistently faster for higher-order modes than for lower-order modes. This trend is ordered along the backbone curves of the frequency-energy plot, with the frequency decreasing as the energy of the system decreases. This is consistent with previous studies of the resonance capture cascade phenomenon [39] occurring in the equipped NES multi-degree-of-freedom system, which have demonstrated that the initial energy corresponding to the lower-order modes tends to exceed the corresponding energy thresholds more easily and thus dissi-

pates for a longer period of time. Also, it is evident that scenario 1 exhibits energy depletion behavior that is not reflected in the backbone curves of the frequency-energy plot. This indicates that in addition to the primary resonance behavior of the 1:1:1:1 frequency ratio, there is also the phenomenon of internal resonance of non-equal frequency ratio, which is specific to the system after the introduction of the nonlinearity.

In addition, to verify whether there is also an energy threshold for the multi-degree-of-freedom system, a certain mode of the structure is excited at different energy levels to observe and compare the energy dissipation of the system. Figures 24 and 25 show the results between the nonlinear system and its derived system for low and high energy excitation of the third mode.

Comparing Figs. 24 and 25, it can be noticed that when the third mode of the system is excited in the low energy state, the nonlinear and linear absorbers behave almost the same way and at this time the energy proportion of the absorber is at a low level. When the third mode of the system is excited at high energy, the time-frequency analysis of the linear system remains constant, with the third mode vibration dominating the energy dissipation. In contrast, the system with the additional non-linear absorber exhibits modal interactions and dissipates energy along the backbone of the FEP. In this case, the energy proportion of the nonlinear vibration absorber is significantly increased and the energy dissipation of the primary structure is accelerated. Therefore, based on the above analysis, it can

be concluded that there is an energy threshold for the nonlinear system and when the modal energy exceeds the threshold, intermodal interactions are triggered in favor of the energy dissipation of the primary structure compared with the linear absorber.

### 5.2 Unground connection scheme

Inerter is a type of two-ended mechanical element, so if conditions prevent one end from being grounded, both ends can be connected to the structure as an alternative. Figure 26 illustrates a non-linearly tuned inerter absorber installed between the second and third degrees of freedom of the structure. In this case, the equations of motion of the system are as Eq. (31).

$$\begin{aligned} \mathbf{M}\ddot{\mathbf{u}} + \mathbf{C}\dot{\mathbf{u}} + \mathbf{K}\mathbf{u} + f_n(\mathbf{u}, u_d)\mathbf{h} &= 0 \\ f_n(\mathbf{u}, u_d) &= k_d(u_3 - u_d) + k_n(u_3 - u_d)^3 \\ &= m_d(\ddot{u}_d - \ddot{u}_2) + c_d(\dot{u}_d - \dot{u}_2) \\ \mathbf{h} &= [0, -1, 1]^T \end{aligned} \tag{31}$$

Figure 27a shows the main backbone curves of the frequency-energy plot of the system (31). The overall shape of the backbone curves is basically the same as the ungrounded system, but the energy values corresponding to the critical points of the transition from straight to curved segments are significantly lower. This illustrates that the nonlinearity of the ungrounded connection is more easily excited. The backbone curves

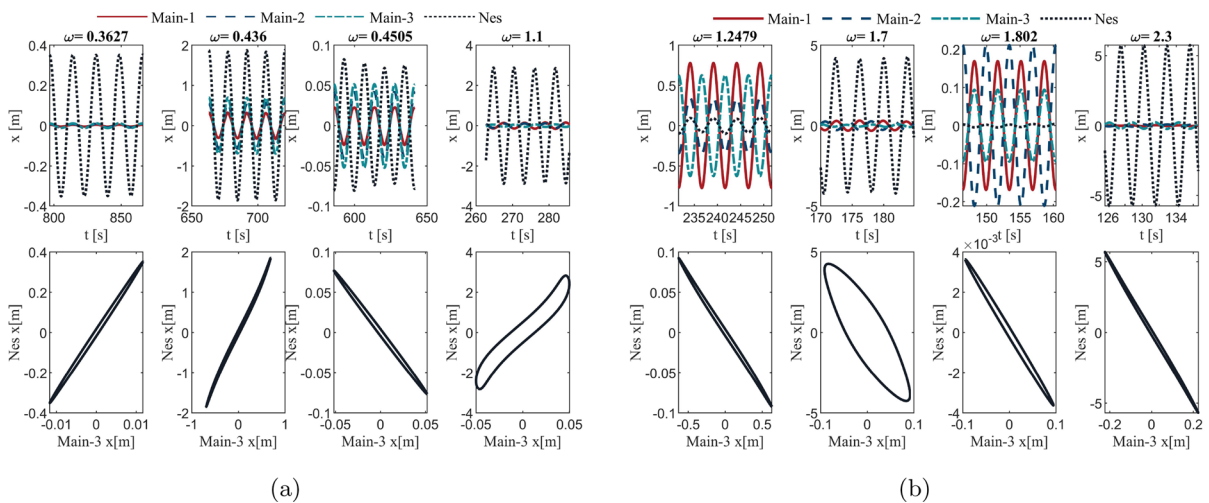
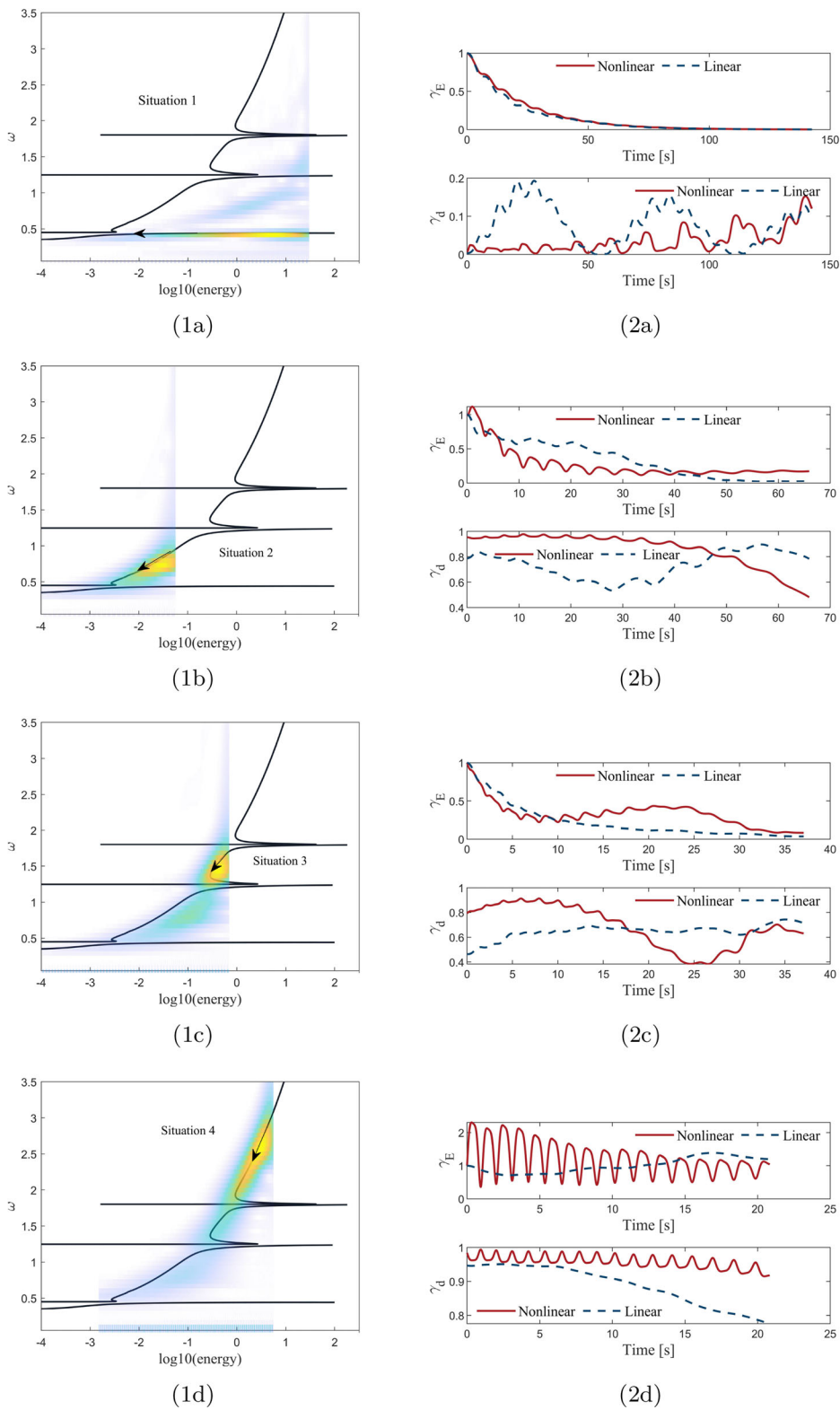
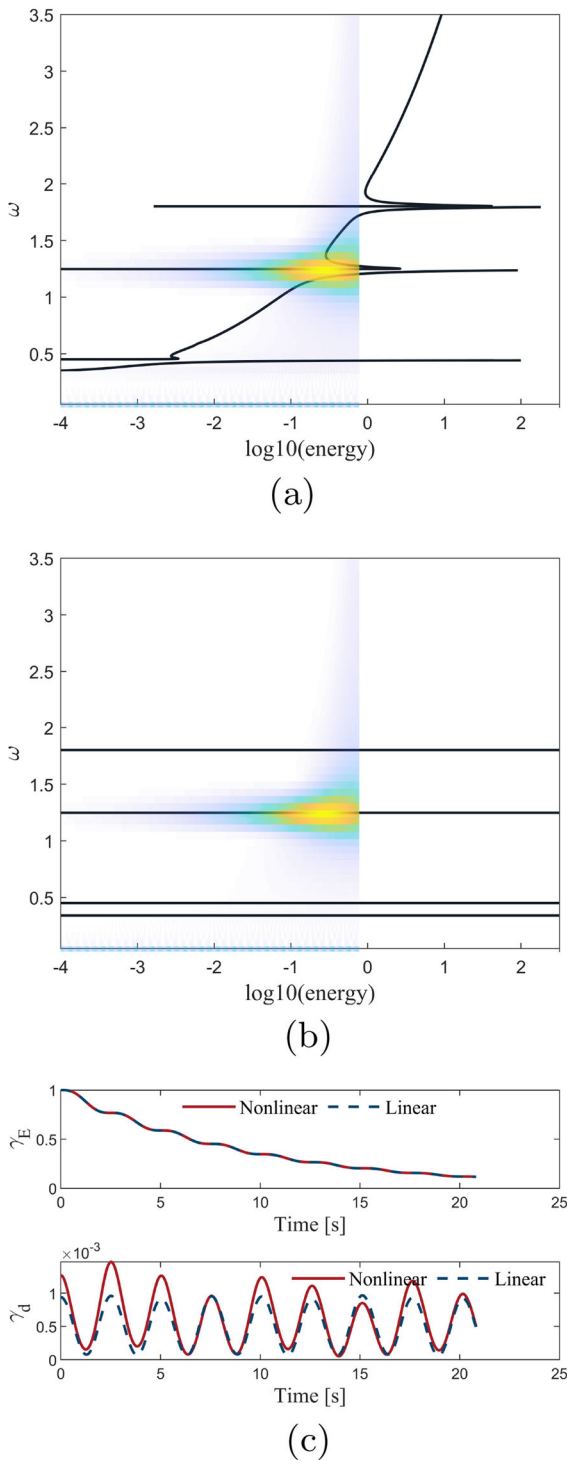


Fig. 22 Schematic periodic motion and configuration diagram of NNM corresponding to frequency



**Fig. 23** Four representative energy dissipation situations (left); Corresponding  $\gamma_E$  and  $\gamma_d$  variations (right)





**Fig. 24** Comparison of energy consumption of non-linear and linear vibration absorbers at low energy input **a** Non-linear time-frequency analysis **b** Linear time-frequency analysis **c** Energy consumption metrics

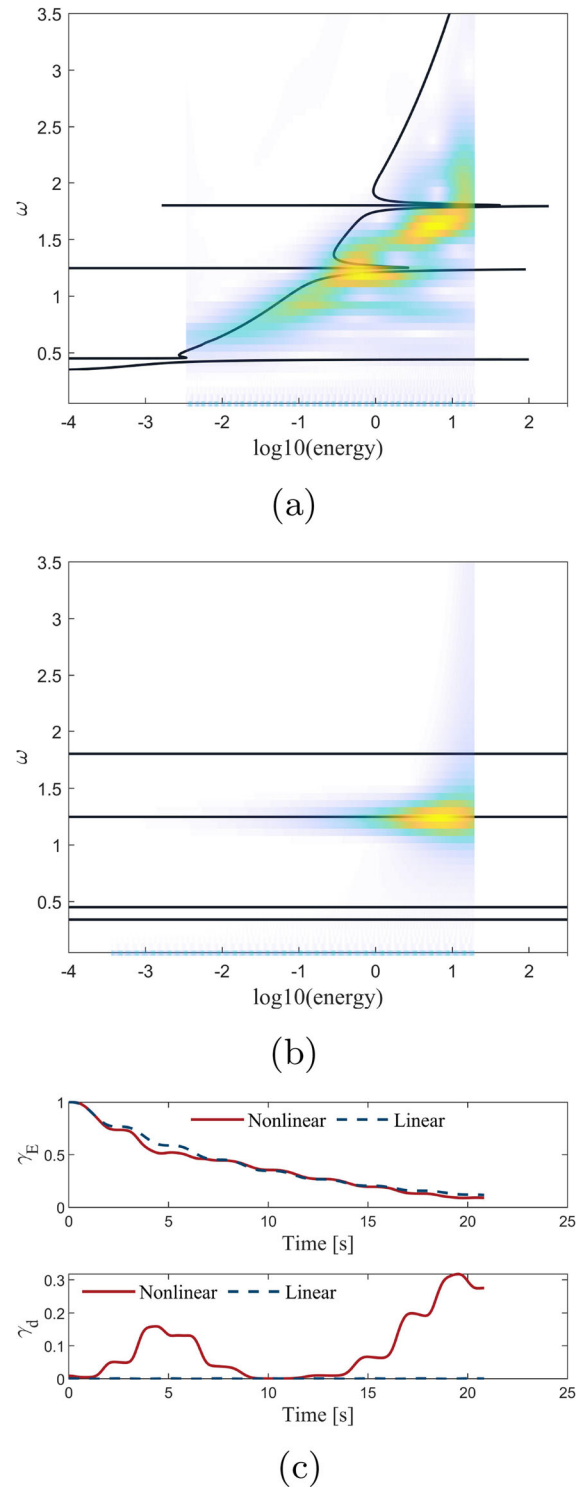


**Fig. 25** Comparison of energy consumption of non-linear and linear vibration absorbers at high energy input **a** Non-linear time-frequency analysis **b** Linear time-frequency analysis **c** Energy consumption metrics

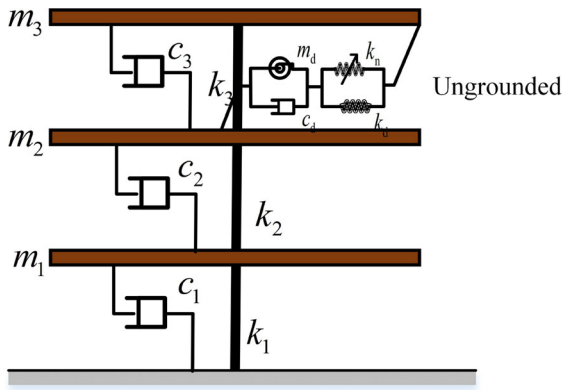


**Fig. 26** Schematic diagram of a MDOF system equipped with ungrounded absorber

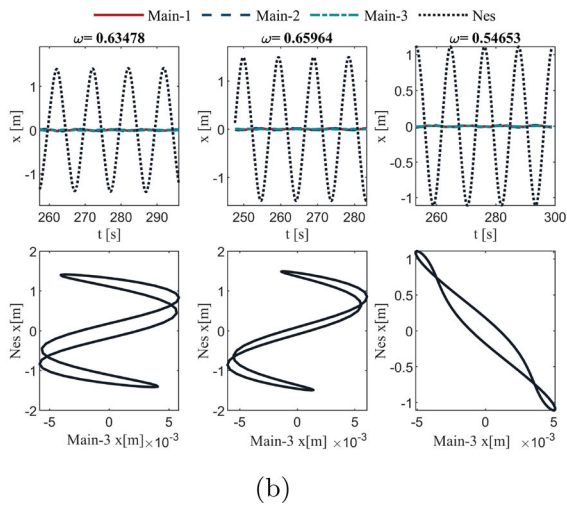
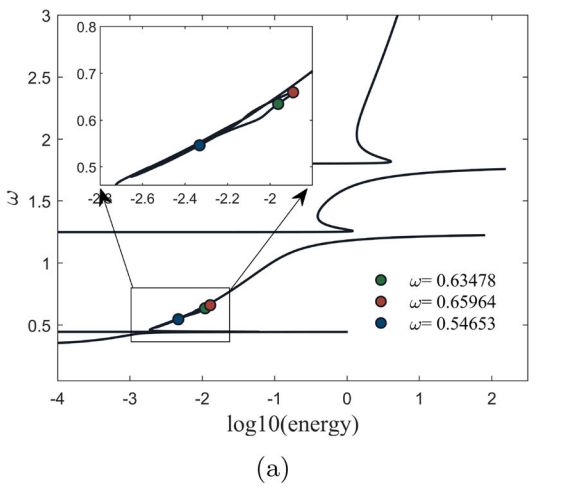
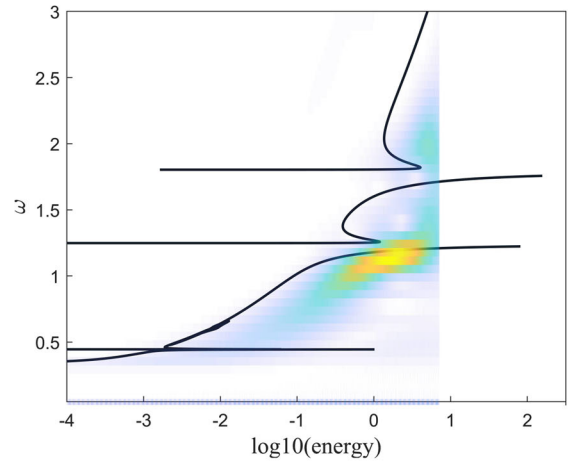
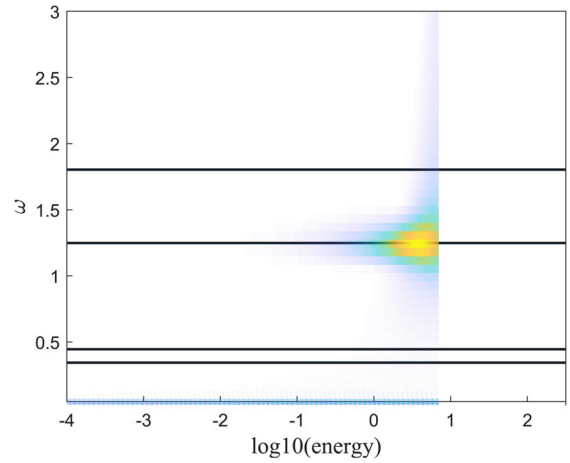


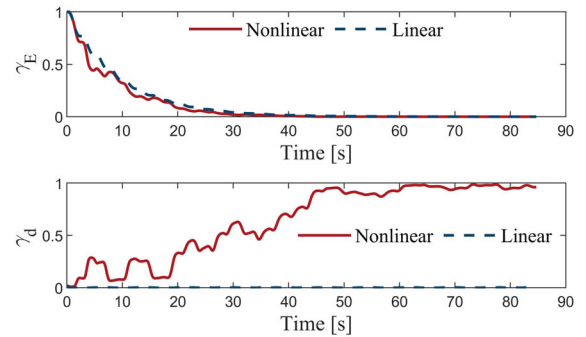
**Fig. 27** The NNM of the system 30 **a** Backbone curves of FEP; **b** periodic motion and configuration diagram on the particular branch



(a)



(b)



(c)

**Fig. 28** Comparison of energy consumption of ungrounded vibration absorbers at high energy input **a** Non-linear time-frequency analysis **b** Linear time-frequency analysis **c** Energy consumption metrics

of the 1:1:1:1 resonance traces the branches of different vibration modes. Figure 27b shows that the vibration frequency of the NES is either 1/2 or 1/3 of that of the primary structure on the particular branch. This indicates that the ungrounded connection may be more susceptible to internal resonance. The performance of the nonlinear absorber is also confirmed by exciting the third mode of the system with high energy input. Figure 28 displays the results of the time-frequency analysis and performance metrics. It is evident that the nonlinear absorber still performs better than the linear absorber when the initial energy input exceeds the energy threshold.

## 6 Conclusion

This paper explores the performance comparison between a nonlinear tuned inerter absorber and the corresponding linear inerter absorber for impact load control. The energy evolution of single and multi-degree of freedom systems equipped with nonlinear absorbers is analyzed and explained in view of slow invariant manifold and nonlinear normal mode. The main conclusions are as follows:

- (1) The slow-flow dynamic analysis of a single-degree-of-freedom system with a nonlinear absorber attached verifies the condition for entering the TET which favors the dissipation of energy from the primary structure: i, The tuned stiffness ratio and damping ratio of the non-linear absorber must satisfy specific conditions to ensure the existence of an invariant manifold bifurcation; ii, the energy input to the system by the impact load must exceed the energy threshold.
- (2) Inspired by the existence of the energy threshold and the high performance of linear tuned absorbers, an optimal design method for the nonlinear stiffness and damping of the nonlinear inerter absorber is proposed. This design method can ensure that TET occurs and effectively improve the performance of nonlinear systems into TET. This enhancement ensures that the nonlinear absorber controls the dynamic response of the primary structure more effectively than the corresponding linearly derived system, and is closer to a tuned linear system under high external initial energy input.
- (3) The existence of the energy threshold is also explained from the NNM point of view using

the time-frequency analysis technique. The critical point on the frequency-energy plot where the vibration frequency begins to increase as the vibration energy increases corresponds to the energy threshold. Compared to linear mode, the vibrational energy on certain branches of nonlinear normal mode is concentrated on the NES, which reveals the reason for the high efficiency of the NES. This localization phenomenon elucidates the rationale behind the enhanced efficiency of non-linear tuned inerter absorber in comparison to linear inerter absorber.

- (4) The transient energy dissipation characteristics of the grounded and ungrounded absorber in a multi-degree-of-freedom system are studied and the existence of an energy threshold for the occurrence of mode interactions is verified. The study found that nonlinearities in the ungrounded connection are more easily activated than in the grounded connection, which results in a lower energy threshold and may be more susceptible to internal resonance. In a few cases, non-linear absorbers may exhibit energy oscillations where the control performance will deteriorate compared to a linear inerter absorber. Nevertheless, in the majority of cases, when the initial energy of the system exceeds the energy threshold corresponding to a specific mode, the efficiency of the nonlinear absorber is found to be higher than that of the corresponding linear system.

**Author contributions** Zijian Yang-Investigation, Conceptualization, Writing, original draft Songtao Xue-Investigation, Conceptualization, Funding acquisition Demin Feng-Investigation, Conceptualization, Funding acquisition Yasuito Sasaki-Funding acquisition, review Liyu Xie-Conceptualization, Funding acquisition, review and editing

**Funding** The authors would like to gratefully acknowledge the support of the National Key R&D Program of China (Grant No.2021YFE0112200) and the Natural Science Foundation of Shanghai (Grant No. 20ZR1461800).

**Data availability** The data that support the findings of this study are available from the corresponding author upon reasonable request.

## Declarations

**Conflict of interest** The authors declare that they have no known competing financial interests or personal relationships that could have appeared to influence the work reported in this paper.

## References

1. Gutierrez Soto, M., Adeli, H.: Tuned mass dampers. *Arch. Comput. Methods Eng.* **20**, 419–431 (2013). <https://doi.org/10.1007/s11831-013-9091-7>
2. Rana, R., Soong, T.: Parametric study and simplified design of tuned mass dampers. *Eng. Struct.* **20**(3), 193–204 (1998). [https://doi.org/10.1016/s0141-0296\(97\)00078-3](https://doi.org/10.1016/s0141-0296(97)00078-3)
3. Smith, M.C.: Synthesis of mechanical networks: the inerter. *IEEE Trans. Autom. Control* **47**(10), 1648–1662 (2002)
4. Hu, Y., Chen, M.Z., Shu, Z.: Passive vehicle suspensions employing inerters with multiple performance requirements. *J. Sound Vib.* **333**(8), 2212–2225 (2014)
5. Smith, M.C., Wang, F.-C.: Performance benefits in passive vehicle suspensions employing inerters. *Veh. Syst. Dyn.* **42**(4), 235–257 (2004)
6. Ikago, K., Saito, K., Inoue, N.: Seismic control of single-degree-of-freedom structure using tuned viscous mass damper. *Earthq. Eng. Struct. Dyn.* **41**(3), 453–474 (2012). <https://doi.org/10.1002/eqe.1138>
7. Lazar, I.F., Neild, S.A., Wagg, D.J.: Using an inerter-based device for structural vibration suppression. *Earthq. Eng. Struct. Dyn.* **43**(8), 1129–1147 (2014). <https://doi.org/10.1002/eqe.2390>
8. Lazar, I., Neild, S., Wagg, D.: Vibration suppression of cables using tuned inerter dampers. *Eng. Struct.* **122**, 62–71 (2016)
9. Dong, X., Liu, Y., Chen, M.Z.: Application of inerter to aircraft landing gear suspension. In: 2015 34th chinese control conference (CCC), pp. 2066–2071. IEEE
10. Sugimura, Y., Goto, W., Tanizawa, H., Saito, K., Nimomiya, T.: Response control effect of steel building structure using tuned viscous mass damper. In: Proceedings of the 15th World conference on earthquake engineering, vol. 9, pp. 24–28
11. Saitoh, M.: On the performance of gyro-mass devices for displacement mitigation in base isolation systems. *Struct. Control. Health Monit.* **19**(2), 246–259 (2012). <https://doi.org/10.1002/stc.419>
12. Swift, S., Smith, M.C., Glover, A., Papageorgiou, C., Gartner, B., Houghton, N.E.: Design and modelling of a fluid inerter. *Int. J. Control* **86**(11), 2035–2051 (2013). <https://doi.org/10.1080/00207179.2013.842263>
13. Wagg, D.J., Pei, J.: Modeling a helical fluid inerter system with time-invariant mem-models. *Struct. Control. Health Monit.* **27**(10), 2579 (2020). <https://doi.org/10.1002/stc.2579>
14. Asai, T., Araki, Y., Ikago, K.: Energy harvesting potential of tuned inertial mass electromagnetic transducers. *Mech. Syst. Signal Process.* **84**, 659–672 (2017). <https://doi.org/10.1016/j.ymssp.2016.07.048>
15. Gonzalez-Buelga, A., Clare, L.R., Neild, S.A., Jiang, J.Z., Inman, D.J.: An electromagnetic inerter-based vibration suppression device. *Smart Mater. Struct.* **24**(5), 055015 (2015). <https://doi.org/10.1088/0964-1726/24/5/055015>
16. Kerschen, G., Kowtko, J.J., McFarland, D.M., Bergman, L.A., Vakakis, A.F.: Theoretical and experimental study of multimodal targeted energy transfer in a system of coupled oscillators. *Nonlinear Dyn.* **47**, 285–309 (2007)
17. Kerschen, G., Lee, Y.S., Vakakis, A.F., McFarland, D.M., Bergman, L.A.: Irreversible passive energy transfer in coupled oscillators with essential nonlinearity. *SIAM J. Appl. Math.* **66**(2), 648–679 (2005)
18. Lee, Y.S., Kerschen, G., Vakakis, A.F., Panagopoulos, P., Bergman, L., McFarland, D.M.: Complicated dynamics of a linear oscillator with a light, essentially nonlinear attachment. *Physica D* **204**(1–2), 41–69 (2005)
19. Vakakis, A.F.: Inducing passive nonlinear energy sinks in vibrating systems. *J. Vib. Acoust.* **123**(3), 324–332 (2001)
20. Vakakis, A.F., Gendelman, O.: Energy pumping in nonlinear mechanical oscillators: part ii-resonance capture. *J. Appl. Mech.* **68**(1), 42–48 (2001)
21. Manevitch, L.I.: Complex Representation of Dynamics of Coupled Nonlinear Oscillators. *Mathematical models of non-linear excitations, transfer, dynamics, and control in condensed systems and other media*, pp. 269–300. Springer, Boston (1999)
22. Gendelman, O., Starosvetsky, Y., Feldman, M.: Attractors of harmonically forced linear oscillator with attached nonlinear energy sink i: description of response regimes. *Nonlinear Dyn.* **51**, 31–46 (2008)
23. Gendelman, O.V.: Bifurcations of nonlinear normal modes of linear oscillator with strongly nonlinear damped attachment. *Nonlinear Dyn.* **37**, 115–128 (2004)
24. Gendelman, O.V., Gourdon, E., Lamarque, C.-H.: Quasiperiodic energy pumping in coupled oscillators under periodic forcing. *J. Sound Vib.* **294**(4–5), 651–662 (2006)
25. Starosvetsky, Y., Gendelman, O.: Strongly modulated response in forced 2dof oscillatory system with essential mass and potential asymmetry. *Physica D* **237**(13), 1719–1733 (2008)
26. Nucera, F., Vakakis, A.F., McFarland, D.M., Bergman, L., Kerschen, G.: Targeted energy transfers in vibro-impact oscillators for seismic mitigation. *Nonlinear Dyn.* **50**, 651–677 (2007)
27. Gendelman, O., Sigalov, G., Manevitch, L., Mane, M., Vakakis, A., Bergman, L.: Dynamics of an eccentric rotational nonlinear energy sink. *J. Appl. Mech.* **79**, 11012 (2012)
28. Sigalov, G., Gendelman, O., Al-Shudeifat, M., Manevitch, L., Vakakis, A., Bergman, L.: Resonance captures and targeted energy transfers in an inertially-coupled rotational nonlinear energy sink. *Nonlinear Dyn.* **69**, 1693–1704 (2012)
29. Andersen, D., Starosvetsky, Y., Vakakis, A., Bergman, L.: Dynamic instabilities in coupled oscillators induced by geometrically nonlinear damping. *Nonlinear Dyn.* **67**, 807–827 (2012)
30. Wang, J., Wierschem, N.E., Spencer, B.F., Jr., Lu, X.: Track nonlinear energy sink for rapid response reduction in building structures. *J. Eng. Mech.* **141**(1), 04014104 (2015)
31. Lu, X., Liu, Z., Lu, Z.: Optimization design and experimental verification of track nonlinear energy sink for vibration control under seismic excitation. *Struct. Control. Health Monit.* **24**(12), 2033 (2017)
32. Wang, F.-C., Su, W.-J.: Impact of inerter nonlinearities on vehicle suspension control. *Veh. Syst. Dyn.* **46**(7), 575–595 (2008)

33. Zhang, Y.-W., Lu, Y.-N., Zhang, W., Teng, Y.-Y., Yang, H.-X., Yang, T.-Z., Chen, L.-Q.: Nonlinear energy sink with inerter. *Mech. Syst. Signal Process.* **125**, 52–64 (2019)
34. Zhang, Z., Lu, Z.-Q., Ding, H., Chen, L.-Q.: An inertial nonlinear energy sink. *J. Sound Vib.* **450**, 199–213 (2019)
35. Zhang, L., Xue, S., Zhang, R., Hao, L., Pan, C., Xie, L.: A novel crank inerter with simple realization: constitutive model, experimental investigation and effectiveness assessment. *Eng. Struct.* **262**, 114308 (2022)
36. Kang, J., Xue, S., Xie, L., Tang, H., Zhang, R.: Multi-modal seismic control design for multi-storey buildings using cross-layer installed cable-bracing inerter systems: part 1 theoretical treatment. *Soil Dyn. Earthq. Eng.* **164**, 107639 (2023)
37. Vaurigaud, B., Ture Savadkoohi, A., Lamarque, C.-H.: Targeted energy transfer with parallel nonlinear energy sinks. Part i: Design theory and numerical results. *Nonlinear Dyn.* **66**, 763–780 (2011)
38. Nguyen, T.A., Pernot, S.: Design criteria for optimally tuned nonlinear energy sinks-part 1: transient regime. *Nonlinear Dyn.* **69**, 1–19 (2012)
39. Dekemele, K., De Keyser, R., Loccufer, M.: Performance measures for targeted energy transfer and resonance capture cascading in nonlinear energy sinks. *Nonlinear Dyn.* **93**, 259–284 (2018)
40. Den Hartog, J.P.: *Mechanical Vibrations*. McGraw-Hill, New York (1956)
41. Rosenberg, R.M.: Normal modes of nonlinear dual-mode systems. *J. Appl. Mech.* **27**, 263–268 (1960)
42. Rosenberg, R.M.: The normal modes of nonlinear n-degree-of-freedom systems. *J. Appl. Mech.* **29**, 7–14 (1962)
43. Shaw, S., Pierre, C.: Non-linear normal modes and invariant manifolds. *J. Sound Vib.* **150**(1), 170–173 (1991)
44. Shaw, S.W., Pierre, C.: Normal modes for non-linear vibratory systems. *J. Sound Vib.* **164**(1), 85–124 (1993)
45. Kerschen, G., Peeters, M., Golinval, J.-C., Vakakis, A.F.: Nonlinear normal modes, part i: a useful framework for the structural dynamicist. *Mech. Syst. Signal Process.* **23**(1), 170–194 (2009)
46. Krack, M., Gross, J.: *Harmonic Balance for Nonlinear Vibration Problems*, vol. 1. Springer, Cham, Switzerland (2019)
47. Peeters, M., Vigué, R., Sérandour, G., Kerschen, G., Golinval, J.-C.: Nonlinear normal modes, part ii: toward a practical computation using numerical continuation techniques. *Mech. Syst. Signal Process.* **23**(1), 195–216 (2009)
48. Seydel, R.: *Practical Bifurcation and Stability Analysis*, vol. 5. Springer, New York (2009)

**Publisher's Note** Springer Nature remains neutral with regard to jurisdictional claims in published maps and institutional affiliations.

Springer Nature or its licensor (e.g. a society or other partner) holds exclusive rights to this article under a publishing agreement with the author(s) or other rightsholder(s); author self-archiving of the accepted manuscript version of this article is solely governed by the terms of such publishing agreement and applicable law.